# Simulation studies of temperature anisotropy driven pair-Alfvén and aperiodic instabilities in magnetized pair plasma

M. E. Dieckmann, D. Folini, A. Bret, R. Walder

# Simulation studies of temperature anisotropy driven pair-Alfvén and aperiodic instabilities in magnetized pair plasma



OPEN ACCESS
IOP Publishing
Plasma Physics and Controlled Fusion
Plasma Phys. Control. Fusion **61** (2019) 085027 (10pp)
https://doi.org/10.1088/1361-6587/ab2b2d

# Simulation studies of temperature anisotropy driven pair-Alfvén and aperiodic instabilities in magnetized pair plasma

**M E Dieckmann[1], D Folini[2], A Bret[3,4] and R Walder[2]**

[1] Department of Science and Technology, Linköping University, SE-60174 Norrköping, Sweden
[2] École Normale Supérieure, Lyon, CRAL, UMR CNRS 5574, Université de Lyon, F-69622 Lyon, France
[3] Universidad de Castilla La Mancha, ETSI Ind, E-13071 Ciudad Real, Spain
[4] Instituto de Investigaciones Energeticas & Aplicadas Ind, Campus Universidad Ciudad Real, Ciudad Real E-13071, Spain

E-mail: mark.e.dieckmann@liu.se

Received 4 December 2018, revised 23 May 2019
Accepted for publication 19 June 2019
Published 5 July 2019

**Abstract**

We compare with one-dimensional particle-in-cell simulations the aperiodically growing instabilities driven by a bi-Maxwellian velocity distribution in unmagnetized electron plasma (Weibel instability) and in pair plasma. The simulation box is aligned with the cool direction. The waves in both simulations evolve towards a circularly polarized non-propagating magnetic structure. Its current and magnetic field are aligned and the structure is in a force-free state. We examine how a background magnetic field $B_0$, which is parallel to the simulation direction, affects the waves in the pair plasma. A weak $B_0$ cannot inhibit the growth of the aperiodically growing instability but it prevents it from reaching the force-free stable state. The mode collapses and seeds a pair Alfvén waves. An intermediate $B_0$ couples the thermal anisotropy to the pair Alfvén mode and propagating magnetowaves grow. The phase speed of the pair of Alfvén waves is increased by the thermal anisotropy. Its growth is suppressed when $B_0$ is set to the value that stabilizes the mirror mode.

Keywords: particle-in-cell simulation, Thermal anisotropy, pair plasma, mirror instability, Weibel instability

(Some figures may appear in colour only in the online journal)

## 1. Introduction

Plasma far from a thermal equilibrium, in which binary collisions between particles are infrequent on the time scales of interest, relaxes via the growth of electromagnetic waves. The growing waves extract energy from a nonthermal feature of the plasma and the waves scatter the charged particles bringing the plasma closer to an equilibrium. We call a plasma collisionless if all instabilities grow and saturate on time scales that are shorter than those of collisional processes.



An electron plasma with an anisotropic temperature distribution is unstable. Weibel [1] considered spatially uniform electrons with a bi-Maxwellian velocity distribution with a temperature that was lower along the direction $\mathbf{d}_c$ than along the two orthogonal ones. The temperature orthogonal to $\mathbf{d}_c$ was isotropic. He showed that the plasma is unstable for the general case that a background magnetic field $\mathbf{B}_0$ is aligned with $\mathbf{d}_c$. He derived the spectrum of the growing waves in the limit $B_0 = |\mathbf{B}_0| = 0$. Weibel found an instability that gives rise to a non-oscillatory exponential (aperiodic) growth of waves over a wide range of wavenumbers $\mathbf{k} \parallel \mathbf{d}_c$. Their magnetic fields are oriented orthogonally to $\mathbf{d}_c$.

A $B_0 \neq 0$ changes the spectrum of undamped modes in the plasma and introduces additional instabilities. The whistler wave instability [2–4] yields propagating waves while the

 

electron mirror instability results in aperiodically growing magnetic fields with a growth rate that peaks for wavevectors $\mathbf{k} \times \mathbf{B}_0 \neq 0$. Its growth rate is typically well below that of the Whistler wave instability [5].

Thermally anisotropic ion distributions can also trigger a mirror instability. An ion mirror instability grows in the magnetohydrodynamic limit if the thermal pressure along $\mathbf{B}_0$ is significantly lower than the perpendicular one and if $B_0 = |\mathbf{B}_0|$ is sufficiently weak [6–13]. Its growth rate peaks at oblique angles between $\mathbf{k}$ and $\mathbf{B}_0$. The ion mirror instability tends to grow faster than the competing ion-cyclotron instability [14] and it is thus frequently observed [5].

Evidence for positrons in astrophysical accretion discs and jets [15] and the creation of clouds of electrons and positrons in the laboratory (see [16] for a review) motivate further studies of instabilities in pair plasma. A pure pair plasma supports a wave spectrum that differs significantly from that of an electron–ion plasma [17–20]. We restrict our attention to waves with $\mathbf{k} \parallel \mathbf{B}_0$. Instabilities in pair plasma with a bi-Maxwellian velocity distribution like that in [1] were discussed in [21, 22]. It turns out that aperiodically growing instabilities exist also in a pure pair plasma. They are not suppressed by a $\mathbf{B}_0 \neq 0$ and compete with a pair Alfvén mode instability.

The aforementioned instabilities may develop in the unstable inner accretion discs of black hole binaries that reached a temperature that is high enough to generate electron-positron pairs [23], in pair jets that flow along a guiding magnetic field [24] and in the transition layers of their internal collisionless shocks [25, 26]. These instabilities can dissipate the energy of the inflowing upstream material in the pair shocks that are thought to exist in energetic astrophysical environments [27]. A better understanding of the conditions under which instabilities driven by bi-Maxwellian velocity distributions develop and how they evolve is also important for the interpretation of the data sets provided by the large simulations in [23, 24].

Here we compare with particle-in-cell (PIC) simulations the evolution of the Weibel instability and of its counterpart in pair plasma, which we call the aperiodically growing instability. Both instabilities drive aperiodically growing waves but Weibel considered only the one driven by electrons. Naming that one Weibel instability allows us to distinguish between both. We compare both instabilities for $B_0 = 0$ and study the effects a $B_0 \neq 0$ has on the instability in pair plasma. All species have a bi-Maxwellian nonrelativistic velocity distribution. The perpendicular temperature is twice as high as the one along $\mathbf{d}_c$. We align $\mathbf{d}_c$ with $\mathbf{B}_0$ and the 1D simulation box. We examine the instability for several values of $B_0$.

The Weibel instability and the aperiodically growing instability for $B_0 = 0$ evolve alike. Their final state is a non-propagating wave with a circularly polarized magnetic field that is stable in our 1D geometry. The magnetic field of this wave structure reaches a force-free equilibrium with the plasma current. A second study considers a value for $B_0$ that leads to an initial growth of the aperiodically growing instability. In time the wave power is shifted to lower wave numbers until it matches one at which pair Alfvén waves can grow. The mode driven by the aperiodically growing instability collapses and launches pair Alfvén modes. The thermal anisotropy is rapidly depleted for this value of $B_0$. Three studies employ values of $B_0$ that destabilize the pair Alfvén mode. The phase speed of the pair Alfvén wave is increased by the thermal anisotropy if its speed is comparable to the thermal speed of the electrons and positrons. We show by means of simulations and for our initial conditions that the value of $B_0$ that suppresses the mirror instability stabilizes also the aperiodically growing mode and the pair Alfvén mode.

This paper is structured as follows. Section 2 summarizes the numerical scheme of a PIC code and presents the initial conditions we selected for the simulations. Section 3 shows the results obtained from the simulations of the instabilities with the electron plasma and with the pure pair plasma for $\mathbf{B}_0 = 0$. Section 4 presents the simulation results for the magnetized plasmas. We summarize our findings in section 5.

## 2. The PIC code and the initial conditions

### 2.1. The code

An electromagnetic PIC code solves Ampère's law and Faraday's law

$$\mu_0 \epsilon_0 \frac{\partial \mathbf{E}}{\partial t} = \nabla \times \mathbf{B} - \mu_0 \mathbf{J}, \tag{1}$$

$$\frac{\partial \mathbf{B}}{\partial t} = -\nabla \times \mathbf{E}, \tag{2}$$

on a numerical grid ($\epsilon_0$, $\mu_0$: vacuum permittivity and permeability). The electric $\mathbf{E}$ field and the magnetic $\mathbf{B}$ field are coupled to the plasma via the current density $\mathbf{J}$. PIC codes approximate the plasma by an ensemble of computational particles (CPs), which have the same charge-to-mass ratio as the particles they represent, and compute $\mathbf{J}$ from the ensemble of all CPs. The CPs evolve under the influence of $\mathbf{E}$ and $\mathbf{B}$. The numerical scheme of the EPOCH code we use (see [28] for a detailed discussion) satisfies Gauss' law and the magnetic divergence law to round-off precision.

### 2.2. Initial conditions

We give the positrons and electrons the density $n_0/2$ in the simulations with the pair plasma. We set the electron density to $n_0$ in the simulation of the electron Weibel instability and consider the ions to be an immobile positively charged background that cancels out the electron charge at the simulation's start. All mobile species have a bi-Maxwellian velocity distribution with a thermal speed $v_1 = \sqrt{k_B T_1/m_e}$ ($k_B$, $m_e$, $T_1$: Boltzmann constant, electron mass and temperature $T_1 = 5$ keV) along $x$ and $v_2 = \sqrt{2}\, v_1$ ($T_2 = 2T_1$) along $y$ and $z$. We align $\mathbf{B}_0$ with $x$ and vary its strength. The ratio between the perpendicular (parallel) thermal pressure and the magnetic pressure of $B_0$ is $\beta_\perp = n_0 k_B T_2 / (B_0^2/2\mu_0)$ ($\beta_\parallel = n_0 k_B T_1 / (B_0^2/2\mu_0)$).

According to [10] the threshold for the mirror instability in a spatially uniform plasma that consists of several species $s$ is

$$\sum_s \beta_{s\perp}\left(\frac{T_{s2}}{T_{s1}} - 1\right) > 1 + \frac{\left(\sum_s \rho_s \frac{T_{s2}}{T_{s1}}\right)^2}{2\sum_s \frac{\rho_s^2}{\beta_{s\parallel}}}. \quad (3)$$

The charge density of species $s$ is $\rho_s$. Its parallel and perpendicular temperatures are $T_{s1}$ and $T_{s2}$ with $T_{s2} > T_{s1}$. The $\beta_{s\perp}$ and $\beta_{s\parallel}$ are the contributions of the species $s$ to $\beta_\perp$and $\beta_\parallel$. Electrons and positrons have identical initial conditions and our simulations will show that they maintain equal values of their anisotropies in time. Their opposite charge densities cancel each other out in the numerator of the second term on the right hand side of equation (3). The contributions $s = e$ (electrons) and $s = p$ (positrons) yield $\beta_{e\perp} + \beta_{p\perp} = \beta_\perp$. Hence the threshold $A$ for the mirror instability of electrons and positrons is $A = T_2/T_1 - 1 = 1/\beta_\perp$ and its growth is limited to $\beta_\perp > A^{-1}$ or $\beta_\perp > 1$ for our initial condition $T_2 = 2T_1$.

We normalize space to $\lambda_s = c/\omega_p$ with the total plasma frequency $\omega_p = (n_0 e^2/m_e \epsilon_0)^{1/2}$ ($e$, $m_e$, $c$: elementary charge, electron mass and light speed). The normalized cyclotron frequency is $\omega_c = eB_0/m_e\omega_p$. Times are normalized to $\omega_p$. Wavenumbers $k$ are normalized to $\lambda_s^{-1}$ and frequencies to $\omega_p$ unless stated otherwise. We normalize $\mathbf{E}$ and $\mathbf{B}$ to $m_e c\omega_p/e$ and $m_e\omega_p/e$ and currents to $en_0c$.

The simulation box resolves the length $L_x = 265$ along $x$ by 2000 grid cells and employs periodic boundary conditions. Reference [29] estimates the maximum wave number $k_m$ that can be destabilized by the electron Weibel instability as $k_m = A^{1/2}$. The corresponding wavelength is $\lambda_m = 2\pi/k_m \ll L_x$ for our initial conditions. We evolve all simulations for a time $t_{\max} = 13\,400$, which we resolve with $10^5$ time steps. A total of $10^3$ CPs per cell resolves the plasma and they are distributed in equal parts over electrons and positrons where appropriate.

## 3. Instabilities in unmagnetized electron plasma and pair plasma

We compare the Weibel instability driven by one electron species with the density $n_0$ with the aperiodically growing instability driven by a pair plasma with the same total density. Figure 1 compares the evolution in time of their box-averaged thermal anisotropies $A(t)$, which are computed for each species separately, their magnetic energy densities $P_B(t) = (\langle B_y^2\rangle_x(t) + \langle B_z^2\rangle_x(t))/(2\mu_0 n_0 k_B T_1)$ and that of $B_y(x, t)$ and $B_z(x, t)$. Brackets with the subscript $x$ denote a spatial average over the entire simulation box.

Magnetic field oscillations have grown in the distributions of $B_y(x, t)$ and $B_z(x, t)$ in both simulations. We observe a rapid growth of small filaments with a wavelength $\lambda \leqslant \lambda_m$ until $t \approx 300$ or $\log_{10}(t) \approx 2.47$ when $P_B(t)$ reaches the value 0.01. Both $A(t)$ and $P_B(t)$ evolve identically in both simulations until then. Filaments merge in time and their growth is tied to a further decrease of $A(t)$ and increase of $P_B(t)$. Both simulations show a continuing growth of $P_B(t)$ in figure 1(f) after the instability saturated at $t \approx 300$.

What is the final state to which the plasma is evolving? Figures 1(a), (b) show that both magnetic field components are practically stationary at late times. The electric field $E_x(x, t)$ is at noise levels (not shown). The corresponding equation of motion for a fluid with the mass density $\rho_m$ and the thermal pressure $p_{\text{th}}$ is

$$\rho_m \frac{\mathrm{d}\mathbf{v}}{\mathrm{d}t} = \mathbf{J} \times \mathbf{B} - \frac{\mathrm{d}p_{\text{th}}}{\mathrm{d}x}. \quad (4)$$

The left-hand term vanishes at late times in both simulations since the fluid is stationary. Studying both terms on the right-hand side will reveal the final state of the unstable modes in our 1D geometry. We examine the final state in the simulation with only electrons. We average $B_y(x, t)$, $B_z(x, t)$, $J_y(x, t)$ and $J_z(x, t)$ over the time interval $12\,700 \leqslant t \leqslant 13\,400$ and denote the averaged quantities by brackets with the subscript $t$. We compute the moduli $B_\perp(x) = (\langle B_y\rangle_t^2(x) + \langle B_z\rangle_t^2(x))^{1/2}$ and $J_\perp(x) = (\langle J_y\rangle_t^2(x) + \langle J_z\rangle_t^2(x))^{1/2}$ and show them in figures 2(a), (b). Almost constant values $B_\perp(x) = 0.02$ and $J_\perp(x) \approx 6 \times 10^{-3}$ are observed for $0 \leqslant x \leqslant 145$ and $155 \leqslant x \leqslant 230$.

We compute the integrals $I_x(x, t) = \int v_x^2 f(x, v_x, t)\mathrm{d}v_x$, $I_y(x, t) = \int v_y^2 f(x, v_y, t)\mathrm{d}v_y$, and $I_z(x, t) = \int v_z^2 f(x, v_z, t)\mathrm{d}v_z$, where $f(x, v_i)$ are the projections of the electron phase space density distribution along the direction $i$. We obtain the effective temperatures $T_x(x, t) = I_x(x, t)/I_x(x, 0)$, $T_y(x, t) = I_y(x, t)/I_x(x, 0)$ and $T_z(x, t) = I_z(x, t)/I_x(x, 0)$, which are normalized to $T_1$. We average them over $12\,700 \leqslant t \leqslant 13\,400$ and show them in figure 2(c). The effective temperature along $x$ has increased at the expense of the perpendicular ones as expected from the curve $A(t)$. A summation of the effective temperatures is proportional to $p_{\text{th}}$ and its value changes only slowly along $x$, which suggests that the thermal pressure gradient in equation (4) is not important. Oscillations of $J_\perp(x)$ and $B_\perp(x)$ at $x \approx 150$ and 240 are tied to different effective temperatures along $y$ and $z$; the electron velocity distribution is not a bi-Maxwellian in both intervals.

Stationary plasma structures and weak thermal pressure variations suggest that $\mathbf{J} \times \mathbf{B} \approx 0$ in equation (4). The latter can be fullfilled by $\pm\mathbf{J} \parallel \mathbf{B}$. Since $B_0 = 0$ cannot change during the simulation time due to geometrical constraints and because the current $J_x(x, t)$ is down to noise levels (not shown) we have to test this condition only for the perpendicular magnetic field and current components.

We compute the complex vector $B_\perp^*(x) = \langle B_y\rangle_t(x) + \mathrm{i}\langle B_z\rangle_t(x) = B_\perp \exp(\mathrm{i}\theta_B(x))$ and extract $\theta_B(x)$. The complex current $J_\perp^*(x) = \langle J_y\rangle_t(x) + \mathrm{i}\langle J_z\rangle_t(x)$ yields the phase angle $\theta_J(x)$ while $-J_\perp^*(x) = -\langle J_y\rangle_t(x) - \mathrm{i}\langle J_z\rangle_t(x)$ has the phase angle $\theta_{-J}(x)$. Figure 2(d) reveals that $\theta_{-J}(x)$ follows $\theta_B(x)$ over the entire left half of the simulation box. We find $\theta_B(x) = \theta_J(x)$ for $150 \leqslant x \leqslant 235$ in the right half of the box shown in figure 2(e). Two domains with force-free magnetic structures have formed which are separated by intervals with particle velocity distributions that deviate locally from a

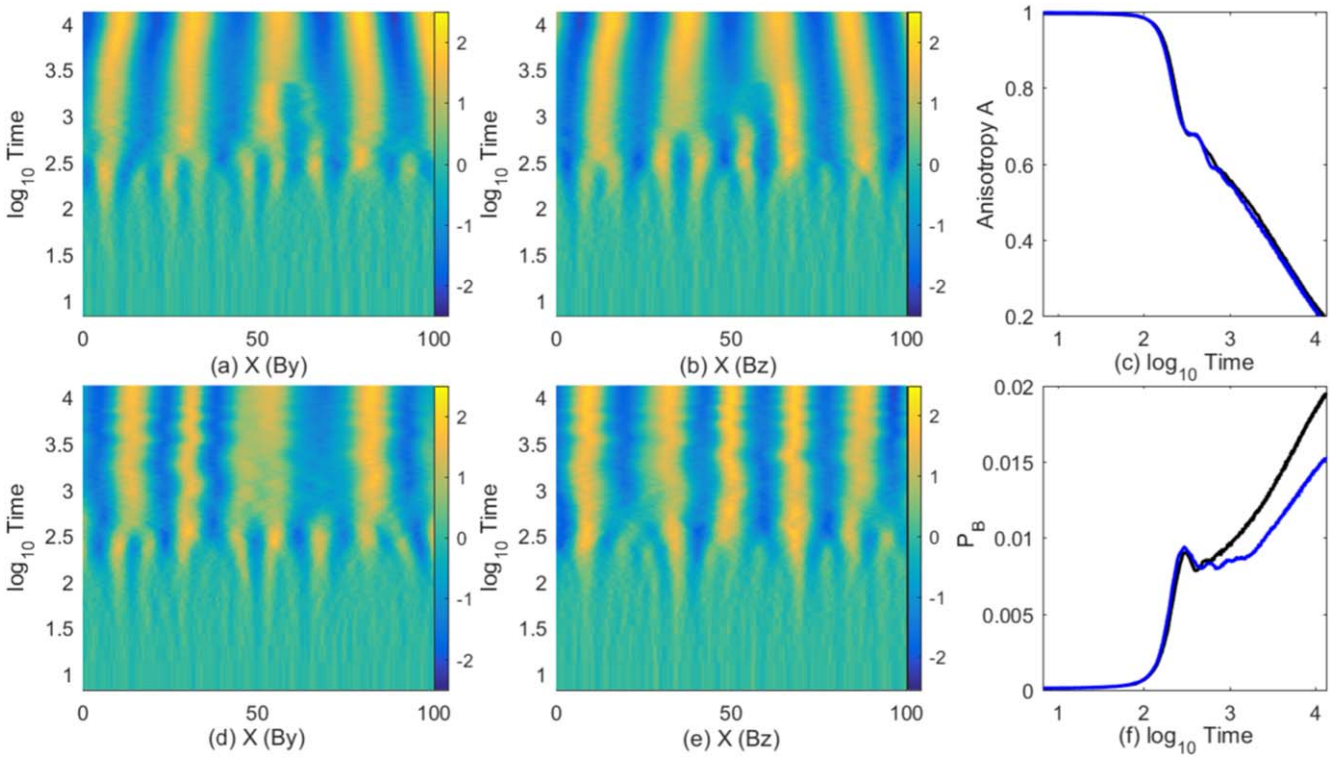


**Figure 1.** The time evolution of the magnetic fields and the thermal anisotropy in the simulations with $B_0 = 0$: panels (a), (b) show the amplitudes of the magnetic $B_y(x, t)$ and $B_z(x, t)$ fields in the simulation with only electrons for $0 \leqslant x \leqslant 100$ multiplied by 100. Panel (c) compares the thermal anisotropy $A(t)$ for the simulation with only electrons (black) to those in the simulation with electrons and positrons, which are both plotted in blue and follow each other closely. Panels (d), (e) show the amplitudes of the magnetic $B_y(x, t)$ and $B_z(x, t)$ fields in the simulation with electrons and positrons for $0 \leqslant x \leqslant 100$ multiplied by 100. Panel (f) compares the magnetic energy density $P_B(t)$ in the simulation with only electrons (black) with that with the pairs (blue).

bi-Maxwellian one. Force-free structures develop also in the simulation with electrons and positrons.

## 4. Magnetized pair plasmas

We examine effects of $B_0 \neq 0$ along $x$ in this section and increase its amplitude in each subsection. We start with $\beta_\perp = 20$, which corresponds to $\omega_c = 1/22.6$. The case $\beta_\perp = 4$ gives $\omega_c = 0.1$, $\beta_\perp = 2$ gives $\omega_c = 0.14$ and $\beta_\perp = 1.5$ gives $\omega_c = 0.163$. Our final study considers values of $B_0$ that are close to the critical $\beta_\perp = 1$ ($\omega_c = 0.2$) that suppresses the mirror instability. The electric field and the current along $\mathbf{B}_0$ remain at noise levels in all simulations, which is a necessary condition for the mirror instability [9].

The pair Alfvén mode is important in our simulations and we summarize some of its properties. Its normalized phase speed is $v_A = B_0/(c^2\mu_0 n_0 m_e)^{1/2}$ in the limit of low wave numbers $k$ provided that all temperatures are non-relativistic and isotropic [22]. Its phase speed decreases with increasing $k$ due to a resonance at the cyclotron frequency. We compare our simulation results to the dispersion relation of the pair Alfvén wave in cold electron–positron plasma derived in [20].

### 4.1. Case $\beta_\perp = 20$

Figures 3(a), (b) depict the initial evolution of $B_y(x, t)$ and $B_z(x, t)$ in the box interval $0 \leqslant x \leqslant 100$ until $t = 3000$. Filaments grow during $0 \leqslant t \leqslant 1500$ in both field components. They damp out after this time and are replaced by low-amplitude waves with a larger wavelength. We compute the spatial power spectrum of the magnetic field $Q(k, t) = |B_y(k, t)|^2 + |B_z(k, t)|^2$, where $B_y(k, t)$ and $B_z(k, t)$ were obtained from the Fourier transforms of $B_y(x, t)$ and $B_z(x, t)$ over $L_x$, and display the result in figure 3(c). Waves grow initially up to the maximum wave number $k_m = 1$ that is unstable to the Weibel instability for $B_0 = 0$.

Figure 3(d) shows that $P_B(t)$ grows approximately exponentially until $t \approx 500$ and saturates at $t = 700$. The wave spectrum in figure 3(c) shifts in time to lower $k$. This shift enables a continuing wave growth as the thermal anisotropy decreases (see figure 3(d)) because $k_m = A^{1/2}$. The modes damp out at $t \approx 2000$ and a wave emerges at $k \approx 0.15$ with an amplitude that remains practically unchanged until the end of the simulation. The modes do not evolve towards a force-free equilibrium because $B_0 \neq 0$. The thermal anisotropy has been depleted at $t \approx 2500$ while $P_B(t)$ decreases by more than an order of magnitude after its initial saturation at the value $8 \times 10^{-3}$.

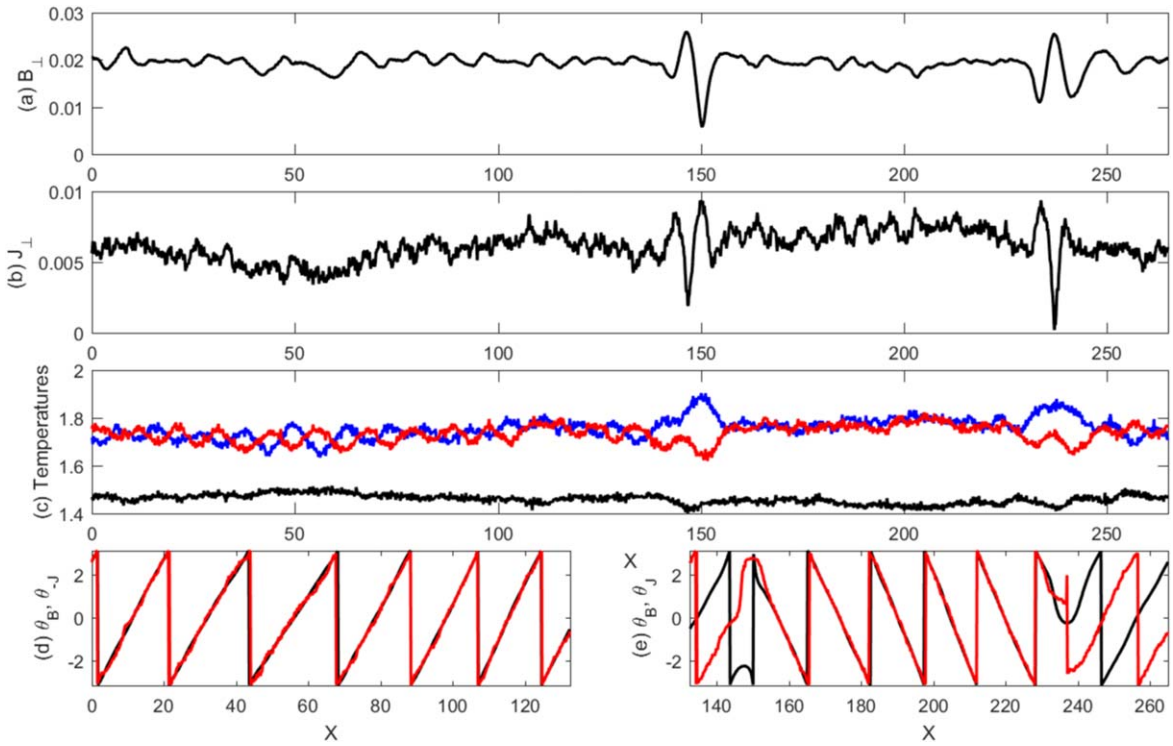


**Figure 2.** The steady-state distribution of the Weibel modes in the simulation with only electrons averaged over the time $12\,700 \leqslant t \leqslant 13\,400$. Panel (a) shows the modulus $B_\perp(x)$ of the perpendicular magnetic field. Panel (b) shows the modulus $J_\perp(x)$ of the perpendicular current. Panel (c) compares the time-averaged effective temperatures $T_x(x)$ (black), $T_y(x)$ (blue) and $T_z(x)$ (red), which are expressed in units of $T_1$. Panel (d) compares the phase $\theta_B(x)$ (black line) of $B_\perp^*(x)$ with the phase $\theta_{-J}(t)$ of the current $-J_\perp^*(t)$ (red line) in the left half of the box. Panel (e) compares $\theta_B(t)$ (black) with $\theta_J(t)$ (red) of $J_\perp^*(t)$ in the right half.

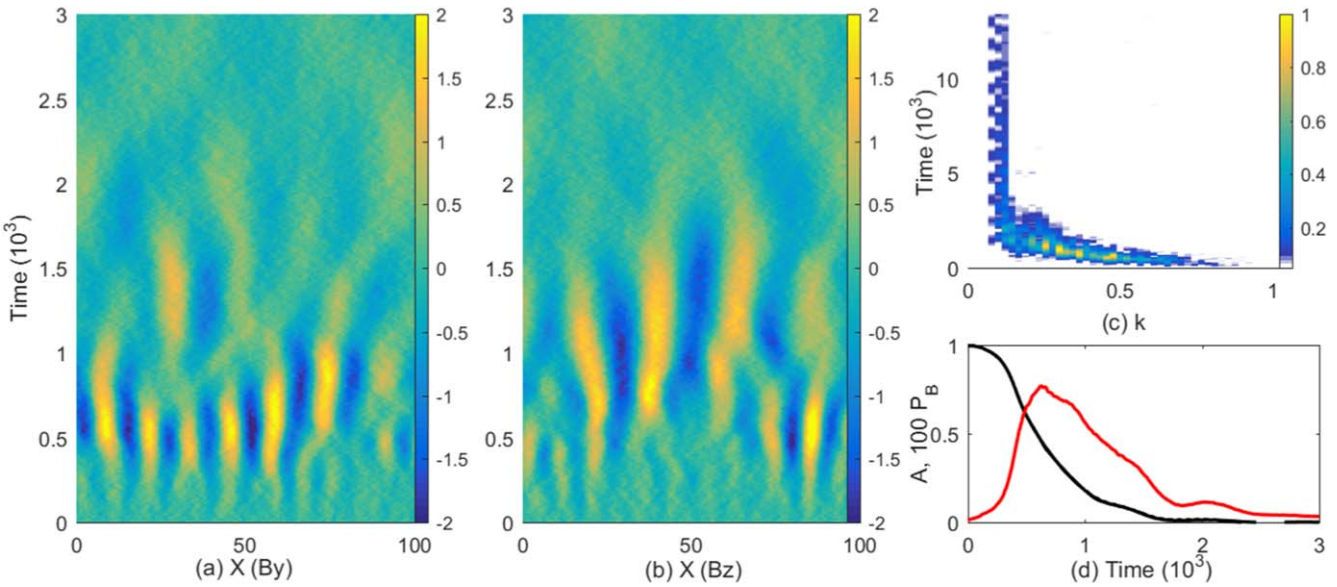


**Figure 3.** The evolution of the magnetic fields in the simulation with $\beta_\perp = 20$. Panel (a) shows the initial evolution of $100B_y$ and (b) that of $100B_z$ in the same spatial sub-interval. Panel (c) displays the spatial power spectrum of the magnetic field $Q(k, t)$, which is normalized to its peak value, while (d) plots $A(t)$ for both particle species (black curves) and $10^2 P_B(t)$ (red curve) until $t = 3000$.

Figure 3(c) reveals oscillations at $k = 0.15$ after $t = 2500$ with a constant amplitude, which suggest the presence of an undamped or weakly damped plasma eigenmode at this $k$. Magnetic oscillations imply that this mode is electromagnetic. Thermal noise spectra can be used to detect eigenmodes [30]. We Fourier transform $B_y(x, t)$ and $B_z(x, t)$ over all $x$ and over suitable time intervals, which gives $B_y(k, \omega)$ and $B_z(k, \omega)$. The spatiotemporal power spectrum of the magnetic field is $FT(k, \omega) = |B_y(k, \omega)|^2 + |B_z(k, \omega)|^2$. We compute this spectrum over $0 \leqslant t \leqslant 3000$ giving

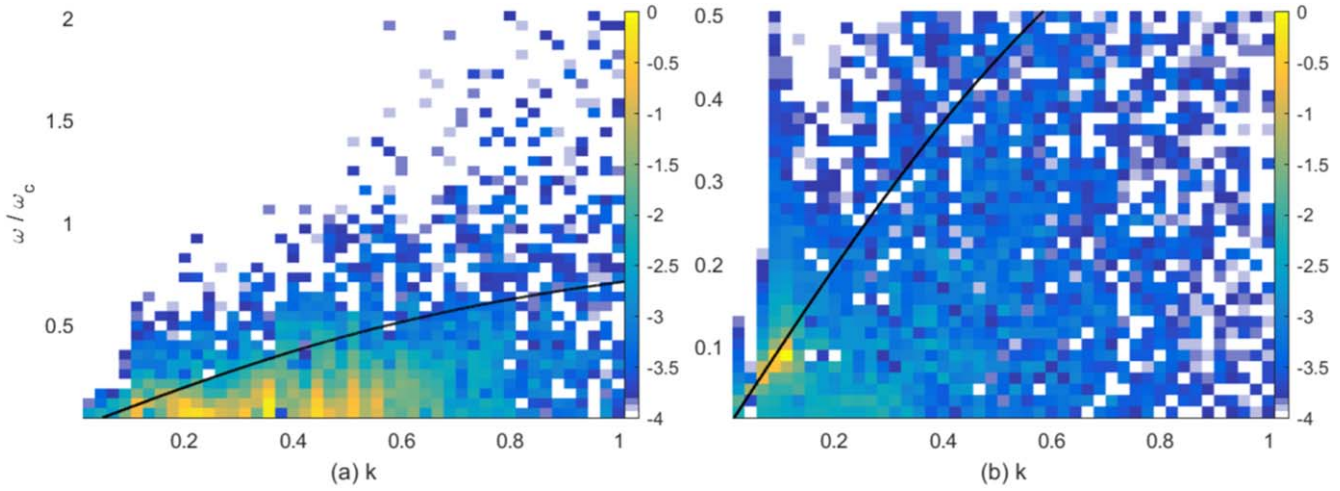


**Figure 4.** Spatiotemporal power spectra of the magnetic field for the simulation with $\beta_\perp = 20$: panel (a) shows $FT_1(k, \omega)$ computed for $0 \leqslant t \leqslant 3000$. Panel (b) displays $FT_2(k, \omega)$ computed for $3000 \leqslant t \leqslant t_{\max}$. Both are normalized to their respective peak values and shown on a 10-logarithmic colour scale. Frequencies are given here in units of the cyclotron frequency $\omega_c = 22.6^{-1}$. The black curves show the dispersion relation of the pair Alfvén mode in cold pair plasma.

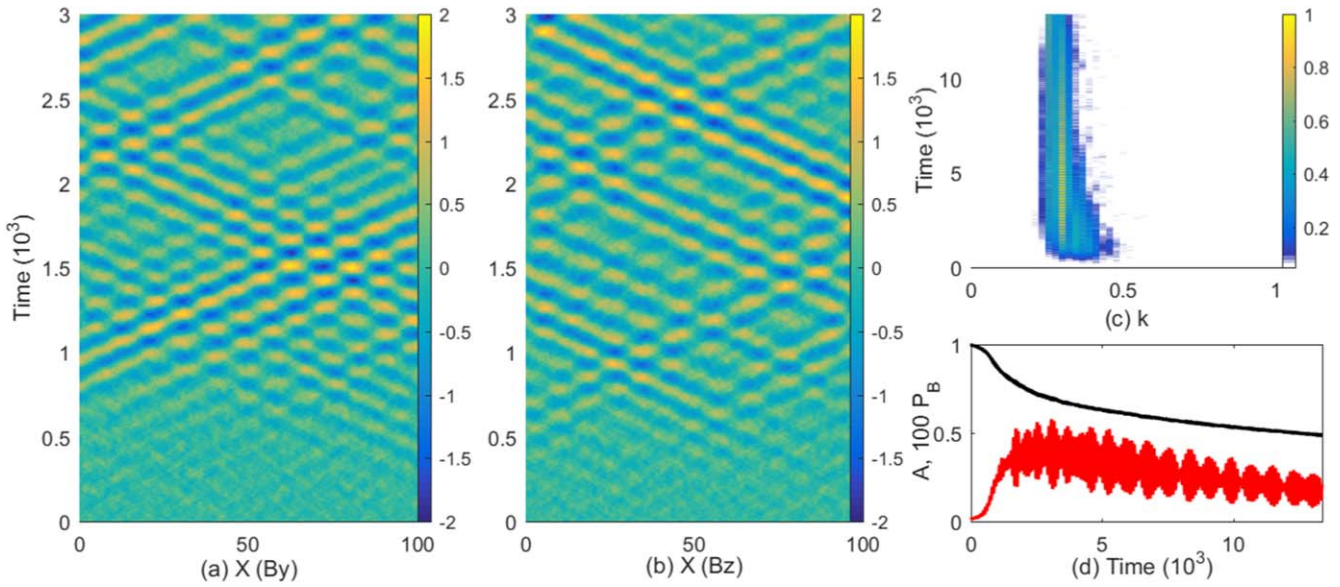


**Figure 5.** The evolution of the magnetic fields in the simulation with $\beta_\perp = 4$. Panel (a) shows the initial evolution of $100B_y$ and (b) that of $100B_z$ in the same spatial sub-interval. Panel (c) displays the spatial power spectrum $Q(k, t)$, which we normalized to its peak value, while (d) plots $A(t)$ of the electrons and positrons (black curves) and $100P_B(t)$ (red curve).

$FT_1(k, \omega)$. The magnetic field data from $3000 \leqslant t \leqslant t_{\max}$ is used to compute $FT_2(k, \omega)$. Both spectra are displayed in figure 4.

According to figure 4(a) most wave power in $FT_1(k, \omega)$ is concentrated at frequencies below $0.3\omega_c$, which corresponds to a normalized frequency 0.013, and $k > 0.2$. These waves are driven by the aperiodically growing instability. We note that the spread of wave power to frequencies $\omega > 0$ in figure 4(a) does not necessarily evidence propagating waves with $\omega/k > 0$. The Fourier spectrum of a function that grows exponentially between two values peaks at $\omega = 0$ but it also stretches out to frequencies $\omega > 0$. Only a signal with a constant amplitude yields a spectrum that is zero for all $\omega \neq 0$. Figure 3(c) demonstrated that these initial waves had damped out at $t \approx 3000$ and gave rise to a stable electromagnetic mode at $k \approx 0.2$. The power peak at $k \approx 0.1$ and the frequency $0.08\omega_c$ in figure 4(b) is located on the dispersion relation of the pair Alfvén mode.

We interpret the evolution of the instability as follows: initially the instability grows at large wave numbers and low $\omega$ and its wave power can not easily couple to the pair Alfvén mode. In time the power peak moves to lower $k$ and eventually the instability drives also the pair Alfvén mode (see also figure 3(c)).

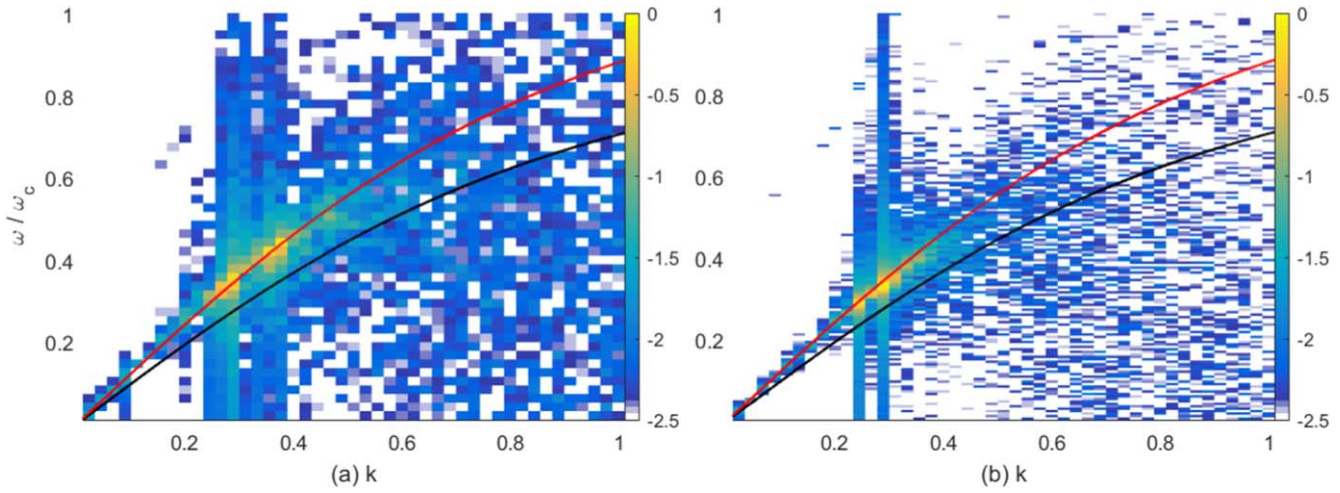


**Figure 6.** Spatiotemporal power spectra of the magnetic field for the simulation with $\beta_\perp = 4$: panel (a) shows the spectrum $FT_1(k, \omega)$ integrated over $0 \leqslant t \leqslant 3000$. Panel (b) displays $FT_2(k, \omega)$, which is integrated over $3000 \leqslant t \leqslant t_{\max}$. Both are normalized to their respective peak values and displayed on a 10-logarithmic color scale. Frequencies are given here in units of the cyclotron frequency $\omega_c = 0.1$. The black curves are the dispersion relation of the pair Alfvén mode in cold plasma. The red curves multiply the frequencies of the black ones by 1.25.

### *4.2. Case $\beta_\perp = 4$*

Figures 5(a), (b) reveals propagating magnetic field structures. They are organized in packets that move in opposite directions. Two strong wave packets cross each other at $t \approx 1500$ and $x \approx 80$ causing wave interference. Figure 5(c) demonstrates that the waves grow in a narrow interval $0.25 \leqslant k \leqslant 0.5$. The anisotropy does not decrease as fast as in the previous case study and the maximum of $P_B(t = 2500) \approx 5 \times 10^{-3}$ is lower.

We subdivide again the data into the interval $0 \leqslant t \leqslant 3000$ with which we compute $FT_1(k, \omega)$. It captures the growth phase of the instability. The second one $3000 \leqslant t \leqslant t_{\max}$ is used to compute $FT_2(k, \omega)$. We show both spatiotemporal power spectra in figure 6 and overplot the dispersion relation of the pair Alfvén mode. Both spectra resemble each other. The power accumulates in both cases in the interval $0.25 \leqslant k \leqslant 0.4$ and at frequencies of about $\omega_c/3$, which corresponds in this case to a normalized frequency $30^{-1}$. The wave spectrum is not monochromatic, which explains why we observe wave packets in figure 5. Their power accumulates above the dispersion relation of the pair Alfvén mode. The pair Alfvén mode has a frequency that exceeds the expected one by the factor 1.25.

We perform three additional simulations in order to test the validity of the solution of the linear dispersion relation in cold pair plasma. They use the same resolution and plasma parameters as the simulation with $\beta_\perp = 4$ except for the temperature. The electrons and positrons have isotropic velocity distributions with the temperatures 100, 5 and 10 keV. We selected the temperatures $T_1 = 5$ keV and $T_2 = 10$ keV in order to demonstrate how strongly the dispersion relation is affected by the temperatures we used in the simulations with a thermally anisotropic plasma. The ratios of the pair Alfvén speed to the plasma's thermal speed are 7, 1 and 0.7, respectively. Figure 7 shows the spatiotemporal power spectrum $FT(k, \omega)$ of the magnetic components $B_y(x, t)$ and $B_z(x, t)$ computed over the full simulation time $0 \leqslant t \leqslant t_{\max}$.

The dispersion relation for the cold pair plasma in figure 7(a) is a good approximation for the magnetic fluctuations up to the frequency $\omega_c/2$ and wave number $k = 0.6$. An increasing temperature reduces the range of wavenumbers that show a pronounced pair Alfvén mode branch. Thermal effects yield a decreasing phase speed of the wave in a narrow $k$-interval and the emergence of broadband fluctations at large $k$, which differs qualitatively from the observed acceleration of the pair Alfvén mode at low $k$ in figure 6.

The pair Alfvén speed in figure 6 is comparable to the thermal speeds of the positrons and electrons and it may thus be affected by a resonance with particles that have an anisotropic velocity distribution. According to equation (60) in [22] a thermal anisotropy can increase the phase speed of the pair Alfvén mode by the factor $\sqrt{(1 + (\tilde{A} - 1)\beta_\parallel)}$, where the thermal anisotropy is defined as $\tilde{A} = T_2/T_1$ in [22] giving $\tilde{A} = A + 1$. This factor equals $\sqrt{3}$ for the case $\beta_\perp = 4$, which exceeds the factor 1.25 in figure 6 by 40%. The decrease of $A$ to 0.6 in figure 5(d) reduces the quantitative mismatch to 20%. Furthermore the finite number of CPs implies that the velocity distribution is a Maxwellian only up to a few times the thermal speed, which is likely to modify the upshift compared to the analytic result in [22].

### *4.3. Cases $\beta_\perp = 2$, 1.5 and 1*

Figure 8(a) shows the spatial power spectrum $Q(k, t)$ of the magnetic field. A wave is growing in the interval $0.3 \leqslant k \leqslant 0.5$. We show the spatiotemporal power spectrum $FT(k, \omega)$, which is integrated over all $0 \leqslant t \leqslant t_{\max}$, in figure 8(b) and overplot the dispersion relation of the pair Alfvén mode in cold plasma. The wave in figure 8(a) is growing on the pair Alfvén wave branch. The noise and the signal follow the overplotted curve up to $k \approx 0.6$. The phase

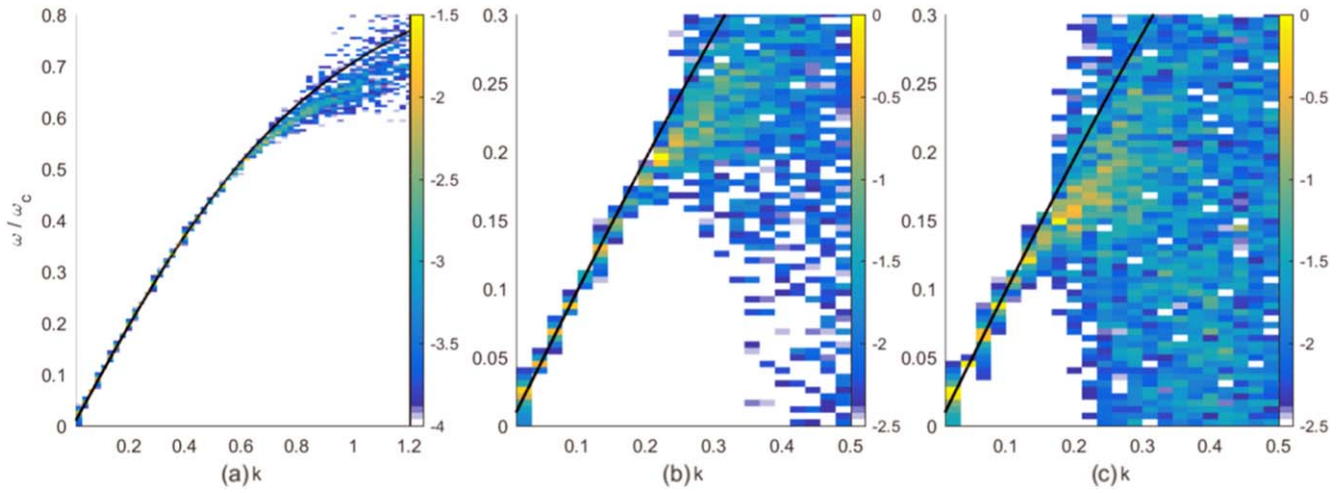


**Figure 7.** The spatiotemporal power spectra $FT(k, \omega)$ of the magnetic field in the test simulations with isotropic temperatures. Panel (a) corresponds to the plasma temperature 100 eV, (b) to the temperature 5 keV (equal to $T_1$) and (c) to the temperature 10 keV (equal to $T_2$). The power spectra are normalized to the peak value in (c) and displayed on a 10-logarithmic color scale. The black curves are the solution of the linear dispersion relation for a cold pair plasma. Frequencies are expressed in units of $\omega_c = 0.1$.

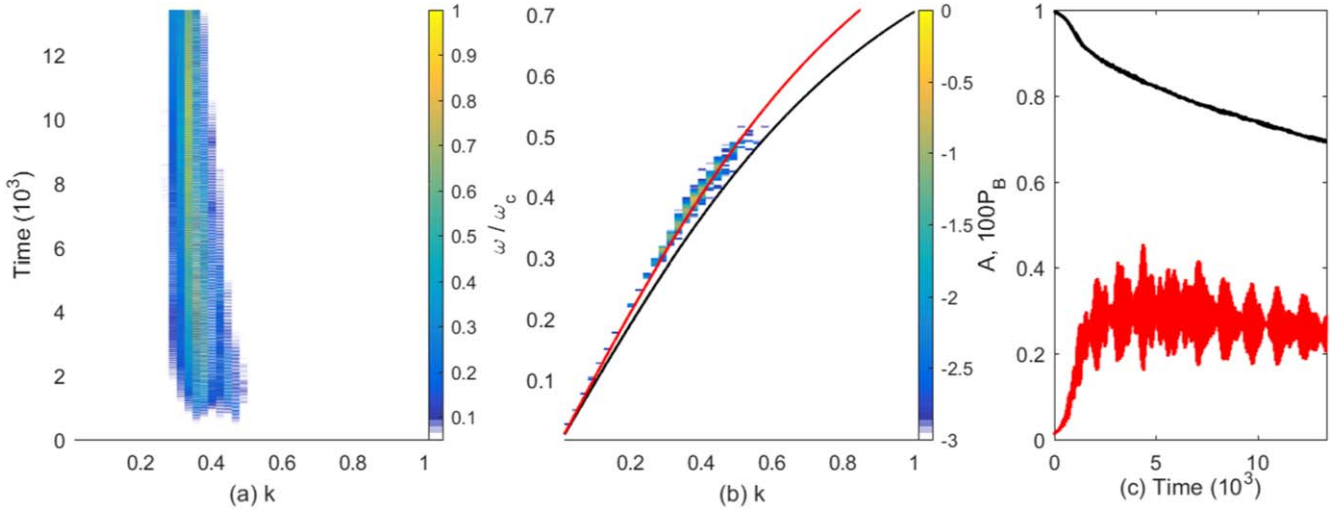


**Figure 8.** The evolution of the magnetic field in the simulation with $\beta_\perp = 2$. Panel (a) shows its spatial power spectrum $Q(k, t)$ and (b) its spatiotemporal power spectrum $FT(k, \omega)$ integrated over $0 \leqslant t \leqslant t_{\max}$. Both are normalized to their respective peak values and the latter is shown on a 10-logarithmic scale. We overplotted the solution of the linear dispersion relation (black curve) of the pair Alfvén mode in cold pair plasma in (b) and a second (red) curve that multiplies the phase speed of the pair Alfvén mode by the factor 1.1. Panel (c) shows the thermal anisotropy $A$ and the magnetic energy density $P_B(t)$ multiplied by 100. Frequencies are expressed in units of $\omega_c = 0.14$.

speed of the pair Alfvén wave in the simulation exceeds the one computed from the cold plasma model by the factor 1.1. The anisotropy $A$ has only been reduced to 0.7 at the simulation's end, which is higher than in the previous case studies, and the maximum value of $P_B(t)$ is lower. The growth of the instability has been slowed down by the low $\beta_\perp$. The decrease in $\beta_\perp$has increased $v_A$ to 1.5 times the thermal speed $v_1$ of particles with the temperature $T_1$. The phase space density of electrons and positrons that can interact resonantly with the pair Alfvén mode has decreased compared to the case $\beta_\perp = 4$.

We decrease the value of $\beta_\perp$below 2. Figure 9 plots $A(t)$ and $P_B(t)$ for the cases $\beta_\perp = 2$, 1.5 and 1 and depicts the spatiotemporal power spectra of the magnetic field $FT(k, \omega)$ integrated over $0 \leqslant t \leqslant t_{\max}$ for values $\beta_\perp = 1.5$ and $\beta_\perp = 1$. The thermal anisotropies $A(t)$ decrease and the magnetic energy densities $P_B(t)$ increase in all three simulations. The decrease of $A(t)$ and the increase of $P_B(t)$ slows down with decreasing $\beta_\perp$. Figure 9(b) suggests an initial exponential growth of $P_B(t)$ in the interval $0 \leqslant t \leqslant 1000$ for the cases $\beta_\perp = 2$ and 1.5, while that of $\beta_\perp = 1$ grows linearly. The growth of the latter could be due to the growth of thermal noise. The value of $v_A$ for $\beta_\perp = 1$ is double the thermal speed of electrons and positrons with the temperature $T_1$. Only a small fraction of the particles can keep up with this pair Alfvén wave and interact resonantly with it, which delays the growth of thermal noise. The dispersion relations of both Alfvén modes computed from the magnetic field distribution in the simulations with $\beta_\perp = 1.5$ and 1 follow closely the solutions of the linear dispersion relation up to $k \approx 0.6$. The

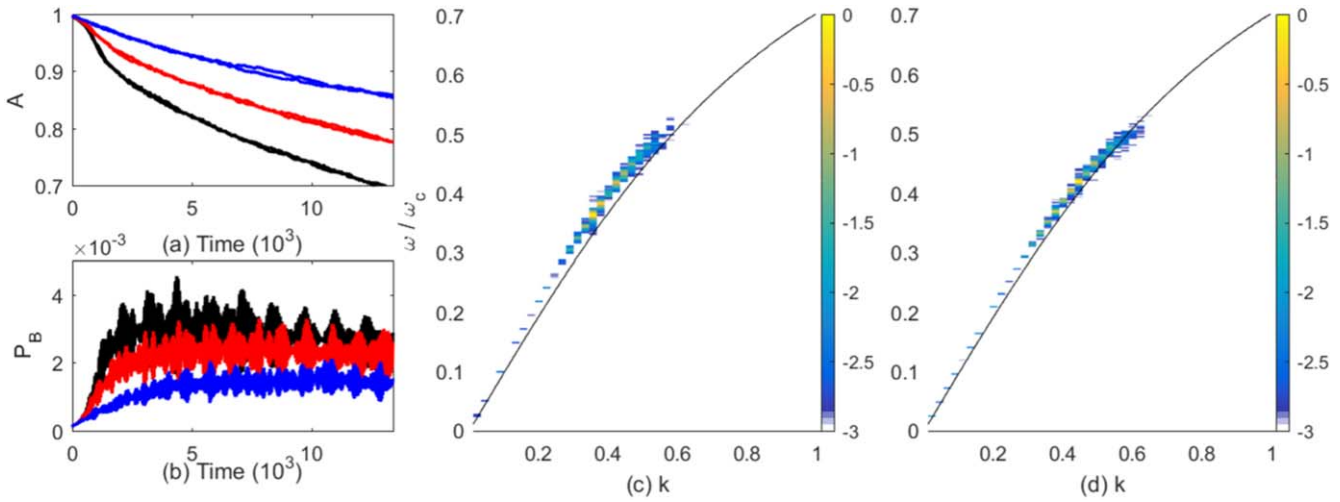


**Figure 9.** Instability in the simulations with $\beta_\perp = 2$, 1.5 and 1: panel (a) compares the time evolution of $A(t)$ for the simulations with $\beta_\perp = 2$ (black curves), $\beta_\perp = 1.5$ (red curves) and $\beta_\perp = 1$ (blue curves). We plot the anisotropies for electrons and positrons separately. The evolution of $P_B(t)$ (same colors) is plotted in panel (b). The spatiotemporal power spectra $FT(k, \omega)$ (integrated over $0 \leqslant t \leqslant t_{\max}$) are depicted in the panels (c), (d) for $\beta_\perp = 1.5$ and 1 respectively. The dispersion relations of the cold pair Alfvén modes are overplotted in (c), (d). Frequencies are expressed in units of $\omega_c = 0.163$ in (c) and $\omega_c = 0.2$ in (d).

phase speed of the pair Alfvén wave in figure 9(c) exceeds the one for a cold plasma by the factor 1.05 and that in figure 9(d) exceeds it by the factor 1.02. A wave speed that decreases with $\beta_\parallel = \beta_\perp/2$ agrees qualitatively with the factor $\sqrt{(1 + (\tilde{A} - 1)\beta_\parallel)}$ in [22].

## 5. Summary

We studied the growth of magnetoinstabilities in an electron plasma with a bi-Maxwellian velocity distribution. We considered the case where one direction was cooler than the ones perpendicular to it, which is the scenario that was studied by Weibel in [1]. We compared this instability to that in a pair plasma with the same distribution and aligned a magnetic field with its cool direction. The cool direction and the magnetic field were parallel to the simulation direction. We obtained the following results.

The Weibel instability grew in the electron plasma and the aperiodically growing instability developed in the pair plasma. Their initial evolution was identical until the growing waves reached a nonlinear amplitude. We observed a continuing growth of the energy density of the magnetic field in both simulations. The final state of the instability in one spatial dimension was that where the currents and the magnetic fields reached a force-free equilibrium. Two configurations were observed: the current was parallel to the magnetic field in one and anti-parallel in the other. Nonlinear modes with different orientations of the current were separated by intervals with a particle velocity distribution that was not a bi-Maxwellian. The numerical value of the magnetic energy density depended on the exact distribution of the nonlinear modes. Nonlinear Weibel modes constitute a circularly polarized electromagnetic wave with vanishing phase and group speeds. Such modes do not exist in the linear regime of a plasma that is not permeated by a background magnetic field (see also [31]).

We studied the impact of a guiding magnetic field, which was aligned with the cool direction, on the instability in the pair plasma. A weak $B_0 \neq 0$ broke the force-free equilibrium and the nonlinear modes collapsed. The wave power shifted in time to lower wavenumbers and it was eventually coupled into the pair Alfvén mode. This coupling led to a particularly fast depletion of the thermal anisotropy. A further increase of $B_0$ quenched the aperiodically growing instability and destabilized the pair Alfvén mode. We showed that the Alfvén mode instability ceased to grow when the amplitude of the magnetic field was set to the value that suppressed the mirror mode. We observed an increased phase speed of the pair Alfvén mode in the simulations in which the pair Alfvén wave grew. This increase was predicted in [22].

It was not evident from the simulation data if the pair-Alfvén wave is driven resonantly by the thermal anisotropy since the magnetic field distribution did not show any obvious phase relation between both perpendicular magnetic field components for $B_0 \neq 0$. We did however observe an increased phase speed of the wave when it was slow enough to interact with particles that streamed along $\mathbf{B}_0$, which suggests that resonant interactions take place. By giving only one species a thermal anisotropy one can drive pair-Alfvén waves via a cyclotron resonance [21]. Our choice of equal distributions for electrons and positrons may have obscured the wave polarization.

Future studies have to examine the stability of the nonlinear Weibel modes in more than one dimension and the exact nature of the aperiodically growing instability in pair plasma for $B_0 \neq 0$. Reference [22] demonstrates that several instabilities compete if the thermal anisotropy of the electrons matches that of the positrons. These are the Weibel modes, the mirror modes and the pair cyctronic modes.

## Acknowledgments

MED acknowledges financial support by a visiting fellowship from the Ecole Nationale Supérieure de Lyon, Université de Lyon. DF and RW acknowledge support from the French National Program of High Energy (PNHE). The simulations were performed with the EPOCH code financed by the grant EP/P02212X/1. The simulations were performed on resources provided by the Swedish National Infrastructure for Computing (SNIC) at the HPC2N in Umeå(project SNIC2018-3-408) and by the French supercomputing facilities GENCI through the grant A0050406960.

## ORCID iDs

M E Dieckmann https://orcid.org/0000-0003-4055-0552

## References

[1] Weibel E S 1959 *Phys. Rev. Lett.* **2** 83
[2] Kennel C F and Petschek H E 1966 *J. Geophys. Res.* **71** 1
[3] Devine P E, Chapman S C and Eastwood J W 1995 *J. Geophys. Res.* **100** 17189
[4] Lazar M, Schlickeiser R and Poedts S 2009 *Phys. Plasmas* **16** 012106
[5] Gary S P and Karimabadi H 2006 *J. Geophys. Res.* **111** A11224
[6] Rudakov L I and Sagdeev R Z 1961 *Dokl. Akad. Nauk. SSSR Engl. Transl.* **6** 415
[7] Southwood D J and Kivelson M G 1993 *J. Geophys. Res.* **98** 9181
[8] Leubner M P and Schupfer N 2001 *J. Geophys. Res.* **106** 12993
[9] Pokhotelov O A, Treumann R A, Sagdeev R Z, Balikhin M A, Onishchenko O G, Pavlenko V P and Sandberg I 2002 *J Geophys. Res.* **107** 1312
[10] Hellinger P 2007 *Phys. Plasmas* **14** 082105
[11] Pokhotelov O A, Sagdeev R Z, Balikhin M A, Fedun V N and Dudnikova G I 2010 *Ann. Geophys.* **28** 2161
[12] Kuznetsov E A, Passot T and Sulem P L 2012 *Phys. Plasmas* **19** 090701
[13] Treumann R A and Baumjohann W 2014 *Nonlin. Processes Geophys.* **21** 143
[14] Gary S P 1992 *J. Geophys. Res.* **97** 8519–29
[15] Siegert T, Diehl R, Greiner J, Krause M G H, Beloborodov A M, Bel M C, Guglielmetti F, Rodriguez J, Strong A W and Zhang X 2016 *Nature* **531** 341
[16] Sarri G, Dieckmann M E, Kourakis I, Di Piazza A, Reville B, Keitel C H and Zepf M 2015 *J. Plasma Phys.* **81** 455810401
[17] Zank G P and Greaves R G 1995 *Phys. Rev.* E **51** 6079
[18] Melrose D B 1997 *Plasma Phys. Controll. Fusion* **39** A93
[19] Munoz V, Asenjo F A, Dominguez M, Lopez R A, Valdivia J A, Vinas A and Hada T 2014 *Nonlin. Processes Geophys.* **21** 217
[20] Keppens R and Goedbloed H 2019 *J. Plasma Phys.* **85** 175850101
[21] Gary S P and Karimabadi H 2009 *Phys. Plasmas* **16** 042104
[22] Schlickeiser R 2010 *Open Plasma Phys. J.* **3** 1
[23] Inchingolo G, Grismayer T, Loureiro N F, Fonseca R A and Silva L O 2018 *Astrophys. J.* **859** 149
[24] Dieckmann M E, Folini D, Hotz I, Nordman A, Dell'Acqua P, Ynnerman A and Walder R 2019 *Astron. Astrophys.* **621** A142
[25] Dieckmann M E and Bret A 2018 *Mon. Not. R. Astron. Soc.* **473** 198
[26] Bret A and Narayan R 2018 *J. Plasma Phys.* **84** 905840604
[27] Marcowith A *et al* 2016 *Rep. Prog. Phys.* **79** 046901
[28] Arber T D *et al* 2015 *Plasma Phys. Controll. Fusion* **57** 113001
[29] Lemons D S, Winske D and Gary S P 1979 *J. Plasma Phys.* **21** 287
[30] Dieckmann M E, Ynnerman A, Chapman S C, Rowlands G and Andersson N 2004 *Phys. Scr.* **69** 456
[31] Krasovsky V L 2010 *Phys. Lett.* A **374** 1751